Shell-Trajectory Measurements
from Direct-Drive–Implosion Experiments

In direct-drive inertial confinement fusion (ICF), laser beams are focused directly onto a fusion capsule that is imploded to reach thermonuclear ignition. The laser beams ablate the target surface and, through the rocket effect, drive the shell to high velocities. Accurate velocity measurements are critical since the minimum total laser energy for ignition is proportional to V_{imp}^{-6}, where V_{imp} is the implosion velocity.[1] Hydrodynamic models show 10% differences in the velocity (~200 km/s) for typical direct-drive implosions on OMEGA.[2,3] To distinguish among models, the velocity must be measured to within an accuracy of 2%. To achieve this accuracy over 200 ps, the radius and time must be measured to within accuracies of ~1 μm and ~5 ps, respectively.

X-ray radiography has long been applied to ICF experiments[4,5] to measure the shell's velocity, but this technique requires backlighter beams that are taken from the 60 OMEGA drive beams, which reduces the available drive beams, thereby reducing the drive symmetry and efficiency. The accuracy of the radial measurements is often dominated by errors in Abel inversion. X-ray radiography is typically possible only when the laser is turned off because the self-emission adds significant noise to the measurements.

In this article, we present a technique[2,3] where the soft x-ray self-emission of a directly driven target is measured with an x-ray framing camera (XRFC)[6,7] and used to determine the trajectory of the imploding shell. A coronal plasma extending from the ablation surface of the imploding shell to the underdense plasma produces a ring of soft x rays that are imaged to the diagnostic plane. With the proper choice of filtration, a combination of the limb effect and an optically thick shell produces an instrument-limited (~5-μm) emission gradient. This steep gradient and the ability to average over many angles enables one to measure the radius of the imploding shell to an accuracy of better than 1 μm. Combined with the well-characterized XRFC timing (an accuracy of ~5 ps over 200 ps), a 2% velocity measurement is obtained.

The diagnostic obtains 16 radial measurements of the shell during the implosion by imaging the x-ray self-emission of the target integrated along the direction of the diagnostic [Fig. 130.62(a)]. A high contrast is observed between the intensity of the surrounding part and the inner part of the images [Fig. 130.62(a)]. The maximum intensity corresponds to the limb effect produced by the x rays emitted by the coronal plasma. When the cold shell reaches significant convergence, it becomes optically thick, absorbing radiation coming from the back of the sphere, which further enhances the contrast. The radius measurement (corresponding to the position of the sharp intensity gradient at the inner circle) is obtained without knowledge of the path-integrated x-ray emission through plasma and absorption through the shell (i.e., no Abel inversion is required and the measurement is insensitive to the x-ray emission profile).

An array of 16 6-μm-diam pinholes are used to produce 16 x-ray images of the target on a four-strip XRFC.[6,7] For optimum resolution, 12× magnification was used with a distance between the target and the detector plane of 38.1 cm. The resolution of the system was calculated by convolving the pinhole with a multichannel plate (MCP)[8] using the ray-tracing program FRED,[9] resulting in an edge spread function that increases from 10% to 90% over 5 μm. The MCP integration time was 40 ps (Ref. 7). The interstrip timing was 200 ps and determined within 5 ps using the Multi-Terawatt laser.[10]

To determine the optimum filtering, Spect3D[11] was used to post-process hydrodynamic simulations of a 20-μm plastic shell implosion and obtain the x-ray emission at the diagnostic plane. Figure 130.62(b) shows the calculated spectrum, at the detector plane, along a line extending from the center of the target ($R = 0$) to beyond the coronal plasma ($R \approx 400$ μm). Three distinct x-ray emission regions are observed with varying contrast: (1) for low photon energies (<250 eV), a narrow, ~50-μm emission region with a medium contrast is observed; (2) for medium photon energies (250 to 500 eV), three distinct
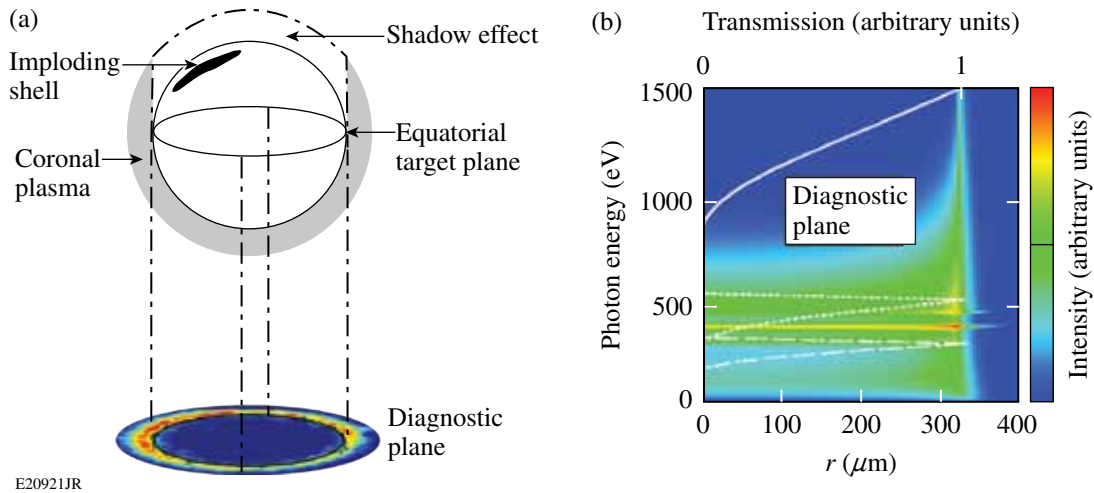
Figure 130.62
(a) Schematic of the limb and shadow effects; (b) simulated spectrally resolved emission at the diagnostic plane integrated along the diagnostic line of sight. The normalized spectral transmission of the low-photon-energy filter (dashed curve), the medium-photon-energy filter (dotted curve), and the high-photon-energy filter (solid curve).

spectral features corresponding to the line emission of the carbon and a low contrast are observed; and (3) for high photon energies (>800 eV), a very thin emission region with a high contrast is observed.

Figure 130.63 shows the results of an experiment performed to investigate the three x-ray-emission regions. The normalized filter transmissions are plotted in Fig. 130.62(b). The low-photon-energy filter used a 3° reflection from Al and transmission through 5-μm-thick parylene N to create a passband filter at ~200 eV. The medium-photon-energy filter used a 3° reflection from Al and transmission through 1-μm-thick vanadium to create a passband filter at ~400 eV. The high-photon-energy filter used 25.4-μm-thick beryllium to create a high-pass filter at ~100 eV. Figure 130.63(c) shows the optimal filtering (with high photon energy) with high contrast, leading to a sharp inner edge to the x-ray emission.

Figure 130.64(a) compares the simulated x-ray emission, spectrally integrated after passing through the high-photon-energy filter, with the corresponding measurements. The location of the middle intensity point in the sharp inner gradient [black curve in Fig. 130.64(c)] is used to determine the shell's radius. After moderate compression, the shell becomes
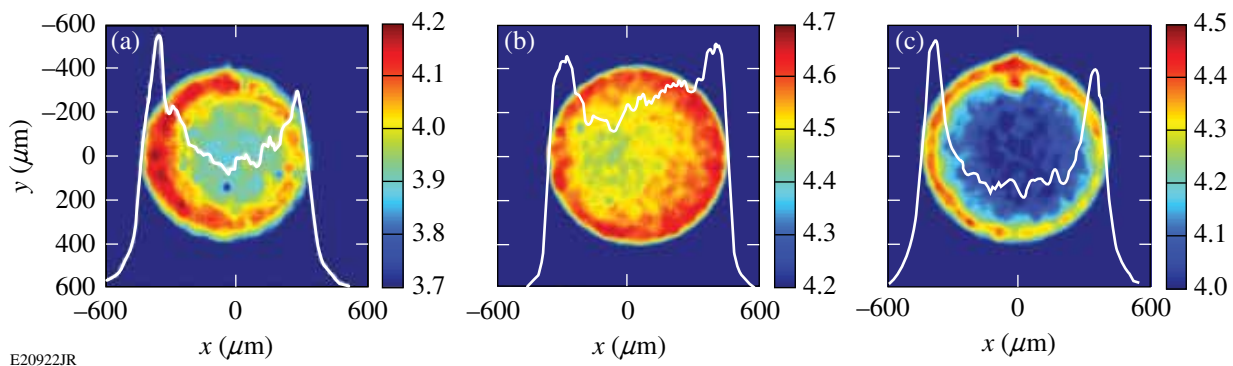

Figure 130.63
Self-emission images and lineouts (white) obtained with the XRFC with a 4× magnification using three different filters: (a) low photon energy; (b) medium photon energy; and (c) high photon energy.
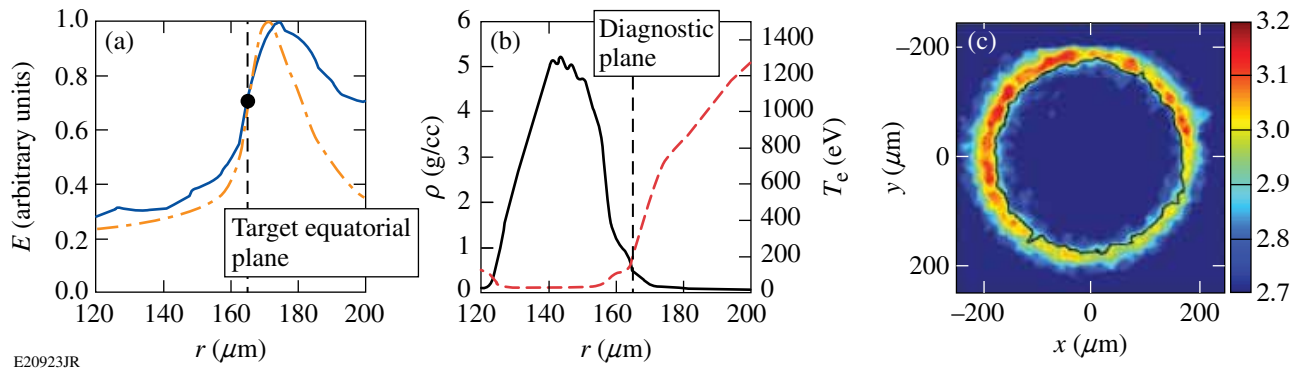
Figure 130.64
(a) Emission at the diagnostic plane obtained by post-processing hydrodynamic simulations and passing through a high-energy filter (orange dashed/dotted line) and experimental emission measured with the XRFC (blue line). The curves are normalized to their maximum values. (b) The calculated electron density (solid black line) and temperature (red dashed line) in the target equatorial plane. (c) Example of an experimental image measured with the XRFC; the black curve corresponds to the curve of the inner gradient, middle intensity point for different angles.

optically thick to x rays above 500 eV, removing the emission from the back of the shell, reducing the signal in the center of the image by a factor of 2, and enhancing the inner gradient [shadow effect represented in Fig. 130.62(a)]. When the laser is on, the middle intensity point corresponds to the ablation surface [Fig. 130.64(b)]. The ablation front follows the mass average point [Fig. 130.65].
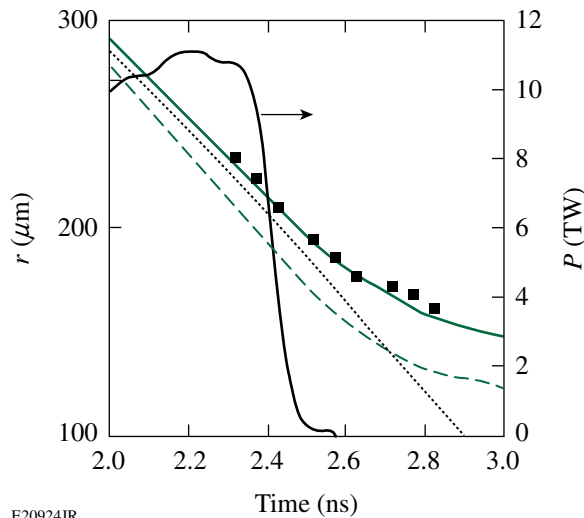
Figure 130.65
Temporal evolution of the laser beams (black solid curve, right axis), shell radius post-processed with Spect3D for simulations with (green solid curve) and without (green dashed curve) cross-beam energy transfer (CBET) and experimental shell trajectories (black squares). For reference, the shell mass averaged point is plotted for the simulations that include CBET (dotted curve). At the end of the laser pulse, the plasma is no longer heated, which results in a decoupling of the x-ray absorption and the shell position.

The accuracy in determining the radius of the middle intensity point is ~3 μm given by σ_n / ρ, where σ_n is the standard deviation of the photon intensity noise and ρ is the slope of the gradient. A standard deviation from the average radius obtained from different angular measurements is 3.5 μm. An accuracy of <1 μm is obtained when averaging the measurements over different angles; this increases the accuracy by a factor of $1/\sqrt{N}$, where N is the number of independent measurements of the radius along different chords passing through the center of the shell (for a shell radius of 150 μm, $\sqrt{N} \sim 10$).

As an example of a use of the diagnostic technique described above, Fig. 130.65 compares the measured and simulated shell trajectories with and without cross-beam energy transfer (CBET) (the experiment is described in detail in Ref. 3). The diagnostic measurements validate the CBET model in *LILAC* simulations.[3] The averaged shell velocity is measured between 2.3 and 2.5 ns to be 200±2 km/s.

REFERENCES

1. M. C. Herrmann, M. Tabak, and J. D. Lindl, Nucl. Fusion **41**, 99 (2001).

2. D. H. Froula, I. V. Igumenshchev, D. T. Michel, D. H. Edgell, R. Follett, V. Yu. Glebov, V. N. Goncharov, J. Kwiatkowski, F. J. Marshall, P. B. Radha, W. Seka, C. Sorce, S. Stagnitto, C. Stoeckl, and T. C. Sangster, Phys. Rev. Lett. **108**, 125003 (2012).

3. I. V. Igumenshchev, W. Seka, D. H. Edgell, D. T. Michel, D. H. Froula, V. N. Goncharov, R. S. Craxton, L. Divol, R. Follett, J. H. Kelly, T. Z. Kosc, P. Michel, R. L. McCrory, A. V. Maximov, D. D. Meyerhofer, J. F. Myatt, T. C. Sangster, A. Shvydky, S. Skupsky, and C. Stoeckl, "Crossed-Beam Energy Transfer in Direct-Drive Implosions," to be published in Physics of Plasmas.

4. D. G. Hicks, B. K. Spears, D. G. Braun, R. E. Olson, C. M. Sorce, P. M. Celliers, G. W. Collins, and O. L. Landen, Phys. Plasmas **17**, 102703 (2010).

5. F. J. Marshall, P. W. McKenty, J. A. Delettrez, R. Epstein, J. P. Knauer, V. A. Smalyuk, J. A. Frenje, C. K. Li, R. D. Petrasso, F. H. Séguin, and R. C. Mancini, Phys. Rev. Lett. **102**, 185004 (2009).

6. D. K. Bradley, P. M. Bell, J. D. Kilkenny, R. Hanks, O. Landen, P. A. Jaanimagi, P. W. McKenty, and C. P. Verdon, Rev. Sci. Instrum. **63**, 4813 (1992).

7. D. K. Bradley *et al.*, Rev. Sci. Instrum. **66**, 716 (1995).

8. V. A. Smalyuk, T. R. Boehly, D. K. Bradley, J. P. Knauer, and D. D. Meyerhofer, Rev. Sci. Instrum. **70**, 647 (1999).

9. Photon Engineering, accessed 9 April 2012, http://www.photonengr.com.

10. V. Bagnoud, I. A. Begishev, M. J. Guardalben, J. Puth, and J. D. Zuegel, Opt. Lett. **30**, 1843 (2005).

11. J. J. MacFarlane *et al.*, High Energy Density Phys. **3**, 181 (2007).